

Bare and stretched string tyre models with distributed FrBD dynamics

Luigi Romano^{*a,b}

^aDivision of Vehicular Systems, Department of Electrical Engineering, Linköping University, SE-581 83 Linköping, Sweden

^bControl Systems Technology Group, Department of Mechanical Engineering, Eindhoven University of Technology,
Groene Loper 1, 5612 AZ Eindhoven, the Netherlands

Abstract

This paper presents a novel class of string tyre models with FrBD friction dynamics. By modelling the distributed carcass and tread deformations with string-like equations, the resulting formulation leads to a system of semilinear parabolic *partial differential equations* (PDEs) that describe the evolution of the tyre states without explicitly distinguishing between stick and slip regimes. Rigorous stability and passivity analyses are also conducted using a Lyapunov-based approach, establishing boundedness of the distributed states and energy dissipation during rolling contact. The proposed Lyapunov function admits a clear physical interpretation as the total elastic energy stored in the tyre, enabling a direct link between mechanical energy storage and frictional dissipation due to slip losses. The steady-state and transient behaviours of the model are investigated both numerically and experimentally, revealing that the new formulation can satisfactorily reproduce nonlinear relaxation phenomena excited by step slip inputs. The resulting model provides a physically interpretable, mathematically well-posed, and computationally efficient basis for advanced vehicle dynamics simulations and control-oriented applications.

Keywords

Tyre dynamics; string tyre models; rolling contact; friction modelling; distributed parameter systems; semilinear systems

1 Introduction

The process of tyre forces and moment generation govern essential vehicle dynamics such as handling, braking, traction, and stability, and its accurate representation is critical for both simulation-based design and advanced control applications [1–14]. Whereas steady-state tyre characteristics are relatively well understood and may be reproduced with high fidelity using empirical and semi-physical models, a reliable description of transient tyre behaviour remains a persistent challenge [15, 16].

Early analytical models, including brush [15–17] and string-like formulations [18–22], have provided a physically interpretable framework for relating the local deformation of the tyre tread and carcass to the resulting forces and moments. These models, which are rooted in rolling contact mechanics and classical friction laws [23], have played a central role in the development of modern tyre theory and continue to underpin widely used semi-empirical formulations [24, 25]. In these descriptions, internal state variables typically represent bristle deflections or distributed contact deformations, leading to systems of hyperbolic PDEs describing the transport of shear stresses along the contact patch [26, 27]. Combined with local Coulomb-Amontons friction laws, similar formulations naturally predict nonlinear relaxation phenomena, and can reproduce experimentally observed delays in force build-up. Nevertheless, their hyperbolic structure imposes intrinsic constraints: boundary conditions cannot be imposed simultaneously at both ends of the contact patch, spatial discontinuities may arise at the leading or trailing edge [15, 20, 21], and oscillatory responses are often observed under time-varying slip excitation. Additionally, Coulomb-like friction models can predict the existence of multiple stick and slip zones within the tyre’s contact

*Corresponding author. Email: luigi.romano@liu.se.

patch [15–17, 20, 21, 26, 27], posing enormous difficulties to the rigorous mathematical analyses of these descriptions. Such features also complicate both numerical implementation, particularly when these models are embedded within vehicle-level simulations.

More recently, the development of dynamic friction models of LuGre [28–36] and FrBD type [37–39] has advanced the modelling of transient tyre-road interaction at the local level. These formulations introduce internal friction states that capture pre-sliding displacement, hysteresis, and velocity-dependent friction effects, and have been successfully applied to tyre dynamics under combined slip and spin conditions. When coupled with distributed contact descriptions, FrBD-based tyre models provide a powerful framework for describing transient rolling contact phenomena without explicitly differentiating between stick and slip behaviours, thus overcoming the intrinsic disadvantages Coulomb friction. However, existing formulations typically retain a transport-dominated structure [37–39], and the influence of tyre structural compliance on the mathematical nature of the governing equations has received limited attention.

In contrast, experimental and numerical evidence indicates that tyre relaxation phenomena cannot be adequately described by pure transport mechanisms. In particular, increasing slip levels are often associated with progressively shorter transients and a pronounced attenuation of high-frequency slip excitations [15, 20, 21, 40]. These observations suggest the presence of diffusive effects within the tyre-road interaction process, arising from the distributed compliance of the tread and carcass, which are not captured by classical hyperbolic formulations without Coulomb-like friction. Motivated by these considerations, this paper introduces the simplest string-based tyre model with distributed FrBD friction, referred to as the *friction with string dynamics* (FrSD) model. The key idea is to combine a nonlocal constitutive description of tyre structural deformation with a dynamic friction law of FrBD type. Unlike traditional brush models, which assume a simple elastic foundation to describe the deflection of bristle elements [15–17], the constitutive relationships adopted in this work explicitly relate internal stresses to spatial derivatives of the deformation field, leading to governing equations that are parabolic for all nonzero slip velocities. This represents a fundamental departure from classical transport-based rolling contact models and has important physical, mathematical, and numerical implications.

Indeed, from a physical standpoint, the parabolic structure naturally introduces diffusive mechanisms that account for relaxation phenomena modulated by the magnitude of the slip and spin inputs. This enables the model to reproduce experimentally observed trends such as faster force build-up at higher slip levels and the suppression of oscillations under high-frequency excitation. From a modelling perspective, the parabolic nature of the equations allows boundary conditions to be imposed simultaneously at both ends of the contact patch, resulting in smooth deformation profiles without artificial kinks at the contact edges. From a systems-theoretic viewpoint, the resulting formulation is well suited for stability analysis and for integration into vehicle-level models, where robustness and numerical reliability are essential.

The main contributions of this work can be summarised as follows:

- (i) The derivation of a novel string-based tyre model with distributed FrBD friction dynamics, grounded in a nonlocal constitutive description of tyre deformation,
- (ii) The identification and analysis of the parabolic character of the resulting governing equations, highlighting its consequences for transient tyre behaviour, including mathematical properties such as stability and passivity,
- (iii) Numerical and experimental validations of both steady-state and transient tyre responses, demonstrating the model’s ability to capture relaxation effects, slip-dependent dynamics, and low-pass filtering behaviour.

The paper is organised as follows. Section 2 introduces the constitutive equations describing tyre structural compliance and the adopted dynamic friction law, derives the governing equations of the FrSD tyre model, and presents expressions for the resulting forces and moments. The mathematical properties of the new string-like formulation are then discussed in Sect. 3, where stability and passivity are studied rigorously. Section 4 illustrates the steady-state and transient behaviour of the model through numerical simulations and experimental validation. Finally, concluding remarks and perspectives for future work are provided in Sect. 5.

Notation

In this paper, \mathbb{R} denotes the set of real numbers; $\mathbb{R}_{>0}$ and $\mathbb{R}_{\geq 0}$ indicate the set of positive real numbers excluding and including zero, respectively. The set of positive integer numbers is indicated with \mathbb{N} ,

whereas \mathbb{N}_0 denotes the extended set of positive integers including zero, i.e., $\mathbb{N}_0 = \mathbb{N} \cup \{0\}$. The set of $n \times m$ matrices with values in \mathbb{F} ($\mathbb{F} = \mathbb{R}, \mathbb{R}_{>0}, \mathbb{R}_{\geq 0}$) is denoted by $\mathbf{M}_{n \times m}(\mathbb{F})$ (abbreviated as $\mathbf{M}_n(\mathbb{F})$ whenever $m = n$). $\mathbf{Sym}_n(\mathbb{R})$ represents the group of symmetric matrices with values in \mathbb{R} ; the identity matrix on \mathbb{R}^n is indicated with \mathbf{I}_n . A positive-definite matrix is noted as $\mathbf{M}_n(\mathbb{R}) \ni \mathbf{Q} \succ \mathbf{0}$; a positive semidefinite one as $\mathbf{M}_n(\mathbb{R}) \ni \mathbf{Q} \succeq \mathbf{0}$. The standard Euclidean norm on \mathbb{R}^n is indicated with $\|\cdot\|_2$; operator norms are simply denoted by $\|\cdot\|$. Given a domain Ω with closure $\overline{\Omega}$, $L^p(\Omega; \mathcal{Z})$ and $C^k(\overline{\Omega}; \mathcal{Z})$ ($p, k \in \{1, 2, \dots, \infty\}$) denote respectively the spaces of L^p -integrable functions and k -times continuously differentiable functions on $\overline{\Omega}$ with values in \mathcal{Z} (for $T = \infty$, the interval $[0, T]$ is identified with $\mathbb{R}_{\geq 0}$). For $\alpha \in (0, 1)$, $C^\alpha(\overline{\Omega}; \mathcal{Z})$ denotes the Banach space of Hölder-continuous functions with values in \mathcal{Z} . $L^2(\Omega; \mathbb{R}^n)$ denotes the Hilbert space of square-integrable functions on Ω with values in \mathbb{R}^n , endowed with inner product $\langle \zeta_1, \zeta_2 \rangle_{L^2(\Omega; \mathbb{R}^n)} = \int_{\Omega} \zeta_1^T(\xi) \zeta_2(\xi) d\xi$ and induced norm $\|\zeta(\cdot)\|_{L^2(\Omega; \mathbb{R}^n)}$. The Hilbert space $H^1(\Omega; \mathbb{R}^n)$ consists of functions $\zeta \in L^2(\Omega; \mathbb{R}^n)$ whose weak derivative also belongs to $L^2(\Omega; \mathbb{R}^n)$. For a function $f : \Omega \mapsto \mathbb{R}$, the sup norm is defined as $\|f(\cdot)\|_{\infty} \triangleq \text{ess sup}_{\Omega} |f(\cdot)|$; $f : \Omega \mapsto \mathbb{R}$ belongs to the space $L^\infty(\Omega; \mathbb{R})$ if $\|f(\cdot)\|_{\infty} < \infty$. A function $f \in C^0(\mathbb{R}_{\geq 0}; \mathbb{R}_{\geq 0})$ belongs to the space \mathcal{K} if it is strictly increasing and $f(0) = 0$; $f \in \mathcal{K}$ belongs to the space \mathcal{K}_∞ if it is unbounded. Finally, a function $f \in C^0(\mathbb{R}_{\geq 0}^2; \mathbb{R}_{\geq 0})$ belongs to the space \mathcal{KL} if $f(\cdot, t) \in \mathcal{K}$ and is strictly decreasing in its second argument, with $\lim_{t \rightarrow \infty} f(\cdot, t) = 0$.

2 Model derivation

The present section is devoted to the derivation of the new FrSD tyre model. The main equations are first introduced in Sect. (2.1), and then combined together in Sect. 2.2 via an application of the *Implicit Function Theorem*.

2.1 Constitutive equations, kinematic constraints, and friction model

The key ingredients for deriving the new string-like description are the constitutive equations, which relate the tyre deformations to the generated forces and moments, the kinematic constraints, linking the sliding and rigid relative velocities to the treadband and carcass deflections, and the friction model. These are described in detail in Sections 2.1.1 and 2.1.2, respectively.

2.1.1 Constitutive differential equations and kinematic constraints

Consider a tyre making contact with the road over a region $\mathcal{C} = \{x \in \mathbb{R} \mid -a \leq x \leq a\}$. The deformation of the tyre treadband and carcass centrelines in the longitudinal and lateral directions may be described by string-like equations of the type [20, 21]

$$\mathbf{S} \frac{\partial^2 \mathbf{u}(x, t)}{\partial x^2} - \mathbf{K} \mathbf{u}(x, t) = -\mathbf{q}(x, t), \quad (x, t) \in (-a, a) \times (0, T), \quad (1)$$

where $\mathbb{R}^2 \ni \mathbf{u}(x, t) = [u_x(x, t) \ u_y(x, t)]^T$ collects the deflections of the tyre treadband and carcass, respectively, $\mathbb{R}^2 \ni \mathbf{q}(x, t) = [q_x(x, t) \ q_y(x, t)]^T$ denotes the force per unit of length acting inside the contact patch, and the matrices $\mathbf{Sym}_2(\mathbb{R}) \ni \mathbf{S} \succ \mathbf{0}$ and $\mathbf{Sym}_2(\mathbb{R}) \ni \mathbf{K} \succ \mathbf{0}$ are given by

$$\mathbf{S} = \begin{bmatrix} EA & 0 \\ 0 & S \end{bmatrix}, \quad (2a)$$

$$\mathbf{K} = \begin{bmatrix} k_x & 0 \\ 0 & k_y \end{bmatrix}, \quad (2b)$$

being $S \in \mathbb{R}_{>0}$ the effective tension of the string, $E \in \mathbb{R}_{>0}$ the Young's modulus, $A \in \mathbb{R}_{>0}$ the cross-sectional area, and $k_x, k_y \in \mathbb{R}_{>0}$ longitudinal and lateral stiffnesses per unit of length [20, 21]. The longitudinal and lateral equations obtained from Eq. (1) are commonly referred to as *bare* and *stretched string tyre models*.

The sliding velocity of the tyre treadband and carcass particles, $\mathbf{v}_s(x, t) \in \mathbb{R}^2$, is given by [16, 17]

$$\begin{aligned} \mathbf{v}_s(x, t) &= \mathbf{v}_r(x, t) + \dot{\mathbf{u}}(x, t) = \mathbf{v}_r(x, t) + \frac{d\mathbf{u}(x, t)}{dt} \\ &= \mathbf{v}_r(x, t) + \frac{\partial \mathbf{u}(x, t)}{\partial t} - V_r(t) \frac{\partial \mathbf{u}(x, t)}{\partial x}, \quad (x, t) \in (-a, a) \times (0, T), \end{aligned} \quad (3)$$

where $\mathbf{v}_r(x, t) \in \mathbb{R}^2$ denotes the rigid relative velocity, and $V_r(t) \in [V_{\min}, V_{\max}]$, with $0 < V_{\min} \leq V_{\max}$, is the *rolling speed* of the tyre.

Together, Eqs. (1) and (3) constitute the first ingredient for the development of the new tyre model. More specifically, Eq. (1) postulates a constitutive relationship linking the deformation $\mathbf{u}(x, t)$ and the force (or stress) $\mathbf{q}(x, t)$, whereas (3) provides the kinematic constraints relating the tyre deflections with the rigid and sliding velocities. To further proceed with the derivation, the following matrices are conveniently introduced:

$$\boldsymbol{\Sigma}_0(x) = \begin{bmatrix} \sigma_{0x}(x) & 0 \\ 0 & \sigma_{0y}(x) \end{bmatrix} \triangleq \frac{\mathbf{K}}{p(x)}, \quad (4a)$$

$$\boldsymbol{\Sigma}_1(x) = \begin{bmatrix} \sigma_{1x}(x) & 0 \\ 0 & \sigma_{1y}(x) \end{bmatrix} \triangleq \frac{\mathbf{S}}{p(x)}, \quad (4b)$$

where $p \in C^1([-a, a]; \mathbb{R}_{>0})$ denotes the vertical pressure distribution inside the tyre's contact patch. Accordingly, the original ODE (1) may be recast as

$$\boldsymbol{\Sigma}_1(x) \frac{\partial^2 \mathbf{u}(x, t)}{\partial x^2} - \boldsymbol{\Sigma}_0(x) \mathbf{u}(x, t) = -\mathbf{f}(x, t), \quad (x, t) \in (-a, a) \times (0, T), \quad (5)$$

where $\mathbb{R}^2 \ni \mathbf{f}(x, t) = [f_x(x, t) \ f_y(x, t)]^T \triangleq \mathbf{q}(x, t)/p(x)$ represents the tangential force per unit of vertical load. The *boundary conditions* (BCs) for both Eqs. (1) and (5) may be formulated by approximating the deflection of the strings by exponentially decreasing functions for $x \in (-\infty, -a]$ and $x \in [a, \infty)$. Accordingly, the following Robin BCs are deduced [15, 20, 21]:

$$\boldsymbol{\Lambda} \frac{\partial \mathbf{u}(a, t)}{\partial x} + \mathbf{u}(a, t) = \mathbf{0}, \quad (6a)$$

$$\boldsymbol{\Lambda} \frac{\partial \mathbf{u}(-a, t)}{\partial x} - \mathbf{u}(-a, t) = \mathbf{0}, \quad t \in (0, T), \quad (6b)$$

where $\mathbf{Sym}_2(\mathbb{R}) \cap \mathbf{GL}_2(\mathbb{R}) \ni \boldsymbol{\Lambda} \succ \mathbf{0}$ collects the *longitudinal* and *lateral relaxation lengths* $\lambda_x, \lambda_y \in \mathbb{R}_{>0}$:

$$\boldsymbol{\Lambda} = \begin{bmatrix} \lambda_x & 0 \\ 0 & \lambda_y \end{bmatrix} \triangleq \begin{bmatrix} \sqrt{\frac{EA}{c_x}} & 0 \\ 0 & \sqrt{\frac{S}{c_y}} \end{bmatrix}. \quad (7)$$

2.1.2 Friction model

In addition to the constitutive relationship (5) and kinematic constraints (3) for the tyre structural elements, it is necessary to specify a local model for the nondimensional friction force $\mathbf{f}_r \in \mathbb{R}^2$ as a function of the sliding velocity. Based on [28, 31], the following relationship is considered in this paper:

$$\mathbf{f}_r(\mathbf{v}_s) = -\frac{\mathbf{M}^2(\mathbf{v}_s) \mathbf{v}_s}{\|\mathbf{M}(\mathbf{v}_s) \mathbf{v}_s\|_{2, \varepsilon}}, \quad (8)$$

where $\varepsilon \in \mathbb{R}_{\geq 0}$ represents a regularisation parameter, $\|\cdot\|_{2, \varepsilon} \in C^0(\mathbb{R}^2; \mathbb{R}_{\geq 0})$ is a regularisation of the Euclidean norm $\|\cdot\|_2$ for $\varepsilon \in \mathbb{R}_{>0}$, often converging uniformly to $\|\cdot\|_2$ in $C^0(\mathbb{R}^2; \mathbb{R}_{\geq 0})$ for $\varepsilon \rightarrow 0$ (e.g., $\|\mathbf{y}\|_{2, \varepsilon} = \sqrt{\|\mathbf{y}\|_2^2 + \varepsilon}$), and with $\|\cdot\|_{2, \varepsilon} \in C^1(\mathbb{R}^2; \mathbb{R}_{\geq 0})$ for $\varepsilon \in \mathbb{R}_{>0}$, and

$$\mathbf{M}(\mathbf{v}_s) = \begin{bmatrix} \mu_x(\mathbf{v}_s) & 0 \\ 0 & \mu_y(\mathbf{v}_s) \end{bmatrix} \quad (9)$$

is a symmetric, positive definite matrix of friction coefficients, i.e., $\mathbf{Sym}_2(\mathbb{R}) \ni \mathbf{M}(\mathbf{y}) \succ \mathbf{0}$ for all $\mathbf{y} \in \mathbb{R}^2$. In this manuscript, it is generally assumed that $\mathbf{M} \in C^0(\mathbb{R}^2; \mathbf{Sym}_2(\mathbb{R}))$ and $\varepsilon \in \mathbb{R}_{>0}$, for reasons that will be clarified in Sect. 2.2.1. For many practical applications, and especially in isotropic conditions, $\mathbf{M}(\mathbf{v}_s)$ may be specified as $\mathbf{M}(\mathbf{v}_s) = \mu(\mathbf{v}_s) \mathbf{I}_2$, where $\mu : \mathbb{R}^2 \mapsto [\mu_{\min}, \infty)$, with $\mu_{\min} \in \mathbb{R}_{>0}$, provides an analytical expression for the friction coefficient. A very common expression for $\mu(\mathbf{v}_s)$ is, for instance,

$$\mu(\mathbf{v}_s) = \mu_d + (\mu_s - \mu_d) \exp\left(-\left(\frac{\|\mathbf{v}_s\|_2}{v_S}\right)^{\delta_s}\right) + \mu_v(\mathbf{v}_s), \quad (10)$$

where $\mu_s, \mu_d \in \mathbb{R}_{>0}$ denote the static and dynamic friction coefficients, $v_S \in \mathbb{R}_{>0}$ indicates the Stribeck velocity, $\delta_S \in \mathbb{R}_{\geq 0}$ the Stribeck exponent, and $\mu_v : \mathbb{R}^2 \mapsto \mathbb{R}_{\geq 0}$ captures the viscous friction.

Combining the constitutive equations (1) with the kinematic constraints (3) and the friction model (8), it is possible to derive the new string-like description of the tyre dynamics. This is addressed next in Sect. 8.

2.2 String tyre model with FrBD dynamics (FrSD)

Starting with Eqs. (1), (3), and (8), Theorem 2.1 will guide the derivation of the governing equations of the FrSD tyre model.

Theorem 2.1 (Edwards [41]). *Suppose that the mapping $\mathbf{H} : \mathbb{R}^{m+n} \mapsto \mathbb{R}^n$ is C^1 in a neighbourhood of a point $(\mathbf{x}^*, \mathbf{y}^*)$, where $\mathbf{H}(\mathbf{x}^*, \mathbf{y}^*) = \mathbf{0}$. If the Jacobian matrix $\nabla_{\mathbf{y}} \mathbf{H}(\mathbf{x}^*, \mathbf{y}^*)^T$ is nonsingular, there exist a neighbourhood \mathcal{X} of \mathbf{x}^* in \mathbb{R}^m , a neighbourhood \mathcal{Y} of $(\mathbf{x}^*, \mathbf{y}^*)$ in \mathbb{R}^{m+n} , and a mapping $\mathbf{h} \in C^1(\mathcal{X}; \mathbb{R}^n)$ such that $\mathbf{y} = \mathbf{h}(\mathbf{x})$ solves the equation $\mathbf{H}(\mathbf{y}, \mathbf{x}) = \mathbf{0}$ in \mathcal{Y} . In particular, the implicitly defined mapping $\mathbf{h}(\cdot)$ is the limit of the sequence $\{\mathbf{h}_k\}_{k \in \mathbb{N}_0}^\infty$ of the successive approximations inductively defined by*

$$\mathbf{h}_{k+1}(\mathbf{x}) = \mathbf{h}_k(\mathbf{x}) - \nabla_{\mathbf{y}} \mathbf{H}(\mathbf{x}^*, \mathbf{y}^*)^{-T} \mathbf{H}(\mathbf{x}, \mathbf{h}_k(\mathbf{x})), \quad (11a)$$

$$\mathbf{h}_0(\mathbf{x}) = \mathbf{y}^*, \quad (11b)$$

for $\mathbf{x} \in \mathcal{X}$.

In order to apply Theorem 2.1, Eq. (5) is first reinterpreted algebraically, that is,

$$\mathbf{f}\left(\mathbf{u}, \frac{\partial^2 \mathbf{u}}{\partial x^2}\right) = \Sigma_0 \mathbf{u} - \Sigma_1 \frac{\partial^2 \mathbf{u}}{\partial x^2}. \quad (12)$$

Subsequently, adopting the notation of Theorem 2.1 and equating Eqs. (12) and (8) gives

$$\mathbf{H}\left(\dot{\mathbf{u}}, \mathbf{u}, \frac{\partial^2 \mathbf{u}}{\partial x^2}, \mathbf{v}_r\right) = \mathbf{f}\left(\mathbf{u}, \frac{\partial^2 \mathbf{u}}{\partial x^2}\right) - \mathbf{f}_r(\mathbf{v}_s(\dot{\mathbf{u}}, \mathbf{v}_r)) = \mathbf{0}, \quad t \in (0, T). \quad (13)$$

In the sliding regime, where $\|\dot{\mathbf{u}}\|_2 \ll \|\mathbf{v}_r\|_2$, Eq. (13) may be approximated by invoking Theorem 2.1 with $\mathbf{x} = (\mathbf{u}, \frac{\partial^2 \mathbf{u}}{\partial x^2}, \mathbf{v}_r)$ and $\mathbf{y} = \dot{\mathbf{u}} = \frac{d\mathbf{u}}{dt}$, yielding

$$\frac{d\mathbf{u}_{k+1}}{dt} = \frac{d\mathbf{u}_k}{dt} - \nabla_{\dot{\mathbf{u}}} \mathbf{H}\left(\dot{\mathbf{u}}^*, \mathbf{u}^*, \frac{\partial^2 \mathbf{u}^*}{\partial x^2}, \mathbf{v}_r^*\right)^{-T} \mathbf{H}\left(\dot{\mathbf{u}}_k, \mathbf{u}_k, \frac{\partial^2 \mathbf{u}_k}{\partial x^2}, \mathbf{v}_r\right), \quad k \in \mathbb{N}_0. \quad (14)$$

In turn, committing the additional approximation [37–39]

$$\nabla_{\dot{\mathbf{u}}} \mathbf{H}\left(\dot{\mathbf{u}}, \mathbf{u}, \frac{\partial^2 \mathbf{u}}{\partial x^2}, \mathbf{v}_r\right)^T \approx \frac{\mathbf{M}^2(\mathbf{v}_s(\dot{\mathbf{u}}, \mathbf{v}_r))}{\left\| \mathbf{M}(\mathbf{v}_s(\dot{\mathbf{u}}, \mathbf{v}_r)) \mathbf{v}_s(\dot{\mathbf{u}}, \mathbf{v}_r) \right\|_{2,\varepsilon}}, \quad (15)$$

recalling Eq. (5) and (12), and truncating Eq. (14) at $k = 1$ provides, for an initial guess $\dot{\mathbf{u}}_0(x) = \mathbf{0}$,

$$\dot{\mathbf{u}}(x, t) = -\mathbf{M}^{-2}(\mathbf{v}_r(x, t)) \left\| \mathbf{M}(\mathbf{v}_r(x, t)) \mathbf{v}_r(x, t) \right\|_{2,\varepsilon} \mathbf{f}(x, t) - \mathbf{v}_r(x, t), \quad (x, t) \in (-a, a) \times (0, T). \quad (16)$$

The above Eq. (16) describes the evolution of the tyre deformations with the rigid relative velocity $\mathbf{v}_r(x, t)$ regarded as the input. A state-space representation of Eq. (16) is introduced next in Sect. 2.2.1, using the travelled distance as independent time-like variable. Before moving to Sect. 2.2.1, an important consideration is formalised in Remark 2.1 below.

Remark 2.1. *For a spatially invariant rigid relative velocity $\mathbf{v}_r^*(x) = \mathbf{v}_r^*$, the adoption of a constant pressure distribution makes the arguments of Theorem 2.1 fully rigorous, since, in this case, it is always possible to find an equilibrium of the type¹*

$$\mathbf{u}^*(x) = -\Sigma_0^{-1} \frac{\mathbf{M}^2(\mathbf{v}_r^*) \mathbf{v}_r^*}{\left\| \mathbf{M}(\mathbf{v}_r^*) \mathbf{v}_r^* \right\|_{2,\varepsilon}}, \quad (17)$$

¹It should be clarified that the expression reported in Eq. (17) will not coincide with the steady-state solution of the FrSD tyre model, even for spatially constant rigid relative velocities.

satisfying

$$\frac{\partial \mathbf{u}^*(x)}{\partial x} = \frac{\partial^2 \mathbf{u}^*(x)}{\partial x^2} = \frac{\partial \mathbf{u}^*(x)}{\partial s} = \mathbf{0}, \quad (18)$$

albeit violating the BCs (6). However, once Eq. (16) has been derived, these unnecessary assumptions may be removed a posteriori, which permits postulating spatially varying rigid relative velocities and pressure distributions $p \in C^1([-a, a]; \mathbb{R}_{>0})$. It is worth noting, however, that compactly supported profiles, such as the parabolic distribution often employed by the brush models, cannot be directly used due to the singularity of $1/p(x)$ at the leading and trailing edges, and need to be regularised first. Alternatively, this limitation may be overcome by connecting the tyre strings in series with additional bristle elements, as done in [22]. Such an extension is also expected to enhance the overall model accuracy and is planned for implementation in future work.

2.2.1 String dynamics

When the spin inputs are moderate, the rigid relative velocity $\mathbf{v}_r(x, t)$ coincides with the slip velocity $\mathbf{v}(x, t) \in \mathbb{R}^2$, given by [38, 39]

$$\mathbf{v}(x, t) = -V_r(t)\boldsymbol{\sigma}(t) - V_r(t)\varphi(t) \begin{bmatrix} 0 \\ x \end{bmatrix}, \quad (19)$$

where $\mathbb{R}^2 \ni \boldsymbol{\sigma}(t) = [\sigma_x(t) \ \sigma_y(t)]^T$ and $\varphi(t) \in \mathbb{R}$ denote the theoretical slip and spin inputs. Therefore, replacing the time variable in Eq. (16) with the travelled distance $\mathbb{R}_{\geq 0} \ni s \triangleq \int_0^t V_r(t') dt'$, the governing PDEs of the FrSD tyre model may be inferred as

$$\frac{\partial \mathbf{u}(x, s)}{\partial s} - \mathbf{\Gamma}(\bar{\mathbf{v}}(x, s), x, s) \frac{\partial^2 \mathbf{u}(x, s)}{\partial x^2} = \frac{\partial \mathbf{u}(x, s)}{\partial x} + \mathbf{\Sigma}(\bar{\mathbf{v}}(x, s), x, s) \mathbf{u}(x, s) - \bar{\mathbf{v}}(x, s), \quad (20a)$$

$$(x, s) \in (-a, a) \times (0, S),$$

$$\mathbf{\Lambda} \frac{\partial \mathbf{u}(a, s)}{\partial x} + \mathbf{u}(a, s) = \mathbf{0}, \quad (20b)$$

$$\mathbf{\Lambda} \frac{\partial \mathbf{u}(-a, s)}{\partial x} - \mathbf{u}(-a, s) = \mathbf{0}, \quad t \in (0, T), \quad (20c)$$

$$\mathbf{u}(x, 0) = \mathbf{u}_0(x), \quad x \in (-a, a), \quad (20d)$$

where $\mathbb{R}_{>0} \ni S \triangleq \int_0^T V_r(t) dt$, the nondimensional rigid slip velocity is defined as $\mathbb{R}^2 \ni \bar{\mathbf{v}}(x, s) = [\bar{v}_x(x, s) \ \bar{v}_y(x, s)]^T \triangleq \mathbf{v}(x, s)/V_r(s)$, and the matrix-valued functions $\mathbf{\Sigma}, \mathbf{\Gamma} : \mathbb{R}^2 \times [-a, a] \times \mathbb{R} \mapsto \mathbf{M}_2(\mathbb{R})$ read

$$\mathbf{\Sigma}(\bar{\mathbf{v}}, x, s) \triangleq \mathbf{\Psi}(\bar{\mathbf{v}}, s) \mathbf{\Sigma}_0(x), \quad (21a)$$

$$\mathbf{\Gamma}(\bar{\mathbf{v}}, x, s) \triangleq -\mathbf{\Psi}(\bar{\mathbf{v}}, s) \mathbf{\Sigma}_1(x), \quad (21b)$$

with $\mathbf{\Psi} : \mathbb{R}^2 \times \mathbb{R}_{\geq 0} \mapsto \mathbf{M}_2(\mathbb{R})$ given by

$$\mathbf{\Psi}(\bar{\mathbf{v}}, s) \triangleq -\frac{1}{V_r(s)} \mathbf{M}^{-2}(V_r(s)\bar{\mathbf{v}}) \left\| \mathbf{M}(V_r(s)\bar{\mathbf{v}}) V_r(s)\bar{\mathbf{v}} \right\|_{2, \varepsilon}. \quad (22)$$

Some considerations about the mathematical structure of the above PDEs (20) are in order. First, in contrast to most rolling contact models employing Coulomb or FrBD-type friction, which are formulated as systems of *hyperbolic* PDEs, Eq. (20) is *parabolic* for all $\varepsilon \in \mathbb{R}_{>0}$. This property follows directly from the constitutive assumption (5), which, by relating the string deformations to the shear stresses via an elliptic operator [22], modifies the underlying hyperbolic structure of classical rolling contact dynamics. This appears to be a new finding and demonstrates that, by injecting higher-order partial derivatives into their governing PDEs, friction can fundamentally alter the mathematical character of rolling contact processes. It is worth noting that, in the limiting case $\bar{\mathbf{v}}(x, s) = \mathbf{0}$ and $\varepsilon = 0$, the matrix $\mathbf{\Gamma}(\bar{\mathbf{v}}(x, s), x, s)$ defined in Eq. (21b) vanishes identically, and Eq. (20) reverts to a hyperbolic system. This degenerate behaviour can be effectively avoided by introducing a strictly positive regularisation parameter $\varepsilon \in \mathbb{R}_{>0}$ in Eq. (8). Besides restoring parabolicity for all inputs, this regularisation enables the establishment of well-posedness results (see, e.g., Sect. 3.1) and facilitates numerical implementation by suppressing spurious instabilities.

Second, beyond improving numerical robustness, the regularisation parameter ε allows both boundary conditions (20b) and (20c) to be imposed simultaneously. This yields a smooth transition between the free portions of the tyre and the contact region, which is physically sound and consistent with empirical evidence, as tread and carcass deformations are known to exhibit smooth spatial profiles. By contrast, owing to their intrinsically hyperbolic nature, classical string models with Coulomb friction must necessarily relax one boundary condition (typically enforcing only Eq. (20b), which leads to the well-known *no-kink* condition at the leading edge).

Third, since the matrix $\mathbf{\Gamma}(\bar{\mathbf{v}}(x, s), x, s)$ in Eq. (21b) depends explicitly on slip and spin inputs, the diffusive term in Eq. (20a) introduces relaxation effects that are directly modulated by the magnitude of these quantities. This feature is again in agreement with experimental observations, which indicates progressively shorter transients as slip levels increase.

2.2.2 Tyre forces and moments

Starting with Eqs. (20) and (1), the tangential forces and the aligning moment acting on the tyre, $\mathbb{R}^2 \ni \mathbf{F}_x(s) = [F_x(s) \ F_y(s)]^T$ and $M_z(s) \in \mathbb{R}$, respectively, may be determined by integration over the contact length, according to

$$\mathbf{F}_x(s) = \int_{-\infty}^{\infty} \mathbf{q}(x, s) dx = \int_{-a}^a \mathbf{q}(x, s) dx, \quad (23a)$$

$$\begin{aligned} M_z(s) &= \int_{-\infty}^{\infty} [xq_y(x, s) - u_y(x, s)q_x(x, s)] dx \\ &= \int_{-a}^a [xq_y(x, s) - u_y(x, s)q_x(x, s)] dx, \quad s \in [0, S]. \end{aligned} \quad (23b)$$

It should be emphasised that a term $u_x(x, s)q_y(x, s)$ has been neglected in the computation of the aligning moment in Eq. (23b), which may be justified by observing that the deformation of the tyre tread is usually small compared to the longitudinal coordinate. Conversely, the contribution $u_y(x, s)q_x(x, s)$ must be included due to the relatively large deflections undergone by the tyre carcass.

Equations (23) may be recast in a more explicit form that is also amenable to mathematical analysis. Specifically, integrating by parts and enforcing the BCs (20b) and (20c) yields

$$\mathbf{F}_x(s) = \int_{-a}^a \mathbf{K}(x)\mathbf{u}(x, s) dx + \mathbf{S}\mathbf{\Lambda}^{-1}\mathbf{u}(a, s) + \mathbf{S}\mathbf{\Lambda}^{-1}\mathbf{u}(-a, s), \quad (24a)$$

$$\begin{aligned} M_z(s) &= \int_{-a}^a xk_y u_y(x, s) dx + \left(a\frac{S}{\lambda_y} + S\right)u_y(a, s) - \left(a\frac{S}{\lambda_y} + S\right)u_y(-a, s) - \int_{-a}^a u_y(x, s)k_x u_x(x, s) dx \\ &\quad - u_y(a, s)\frac{EA}{\lambda_x}u_x(a, s) - u_y(-a, s)\frac{EA}{\lambda_x}u_x(-a, s) - \int_{-a}^a EA \frac{\partial u_y(x, s)}{\partial x} \frac{\partial u_y(x, s)}{\partial x} dx, \quad s \in [0, S]. \end{aligned} \quad (24b)$$

Equations (20) and (24) completely characterise the FrSD tyre model. Its mathematical properties are studied next in Sect. 3.

3 Mathematical properties

The present section is devoted to the mathematical analysis of the FrSD model described by Eqs. (20) and (24). More specifically, Sect. 3.1 investigates well-posedness properties, whereas stability and passivity constitute the main subject of Sect. 3.2.

3.1 Well-posedness

Existence and uniqueness properties for the solution of the PDE (20) may be proved within different functional settings. For simplicity, the following analysis focuses on sufficiently regular solutions, for which well-posedness can be established by invoking standard results already available from the literature. To this end, it is profitable to define the following functions:

$$\tilde{\Sigma}(x, s) \triangleq \Sigma(\bar{\mathbf{v}}(x, s), x, s), \quad (25a)$$

$$\tilde{\mathbf{\Gamma}}(x, s) \triangleq \mathbf{\Gamma}(\bar{\mathbf{v}}(x, s), x, s), \quad (25b)$$

$$\tilde{\mathbf{h}}(x, s) \triangleq \bar{\mathbf{v}}(x, s), \quad (25c)$$

so that the PDE (20) may be recast as

$$\frac{\partial \mathbf{u}(x, s)}{\partial s} - \tilde{\mathbf{\Gamma}}(x, s) \frac{\partial^2 \mathbf{u}(x, s)}{\partial x^2} = \frac{\partial \mathbf{u}(x, s)}{\partial x} + \tilde{\mathbf{\Sigma}}(x, s) \mathbf{u}(x, s) + \tilde{\mathbf{h}}(x, s), \quad (x, s) \in (-a, a) \times (0, S), \quad (26a)$$

$$\mathbf{\Lambda} \frac{\partial \mathbf{u}(a, s)}{\partial x} + \mathbf{u}(a, s) = \mathbf{0}, \quad (26b)$$

$$\mathbf{\Lambda} \frac{\partial \mathbf{u}(-a, s)}{\partial x} - \mathbf{u}(-a, s) = \mathbf{0}, \quad s \in (0, S), \quad (26c)$$

$$\mathbf{u}(x, 0) = \mathbf{u}_0(x), \quad x \in (-a, a). \quad (26d)$$

The more compact representation (26) permits recovering well-posedness invoking the results contained in [42]. In particular, for every $\alpha \in (0, 1)$, the following spaces are conveniently defined:

$$C^{\alpha, 0}([-a, a] \times [0, S]; \mathbb{R}^2) \triangleq \left\{ \mathbf{f} \in C^0([-a, a] \times [0, S]; \mathbb{R}^2) \mid \mathbf{f}(\cdot, s) \in C^\alpha([-a, a]; \mathbb{R}^2), s \in [0, S] \right\}, \quad (27a)$$

$$C^{2, 1}([-a, a] \times [0, S]; \mathbb{R}^2) \triangleq \left\{ \mathbf{f} \in C^0([-a, a] \times [0, S]; \mathbb{R}^2) \mid \frac{\partial \mathbf{f}}{\partial t}, \frac{\partial^2 \mathbf{f}}{\partial x^2} \in C^0([-a, a] \times [0, S]; \mathbb{R}^2) \right\}, \quad (27b)$$

$$C^{2, 1+\alpha}([-a, a] \times [0, S]; \mathbb{R}^2) \triangleq \left\{ \mathbf{f} \in C^{2, 1}([-a, a] \times [0, S]; \mathbb{R}^2) \mid \frac{\partial \mathbf{f}}{\partial t}, \frac{\partial^2 \mathbf{f}}{\partial x^2} \in C^{\alpha, 0}([-a, a] \times [0, S]; \mathbb{R}^2) \right\}. \quad (27c)$$

Theorem 3.1 enounces existence and uniqueness results for regular solutions of Eq. (26).

Theorem 3.1 (Existence and uniqueness of regular solutions). *For all $\tilde{\mathbf{\Sigma}} \in C^1([-a, a] \times [0, S]; \mathbf{M}_2(\mathbb{R}))$ and $\tilde{\mathbf{h}} \in C^1([-a, a] \times [0, S]; \mathbb{R}^2)$ as in Eq. (25), and ICs $\mathbf{u}_0 \in C^{2+\alpha}([-a, a]; \mathbb{R}^2)$, $\alpha \in (0, 1)$, satisfying the BCs (26b) and (26c), the PDE (26) admits a unique regular solution $\mathbf{u} \in C^{2, 1+\alpha}([-a, a] \times [0, S]; \mathbb{R}^2)$ that also satisfies the BCs (26b) and (26c).*

Proof. See Theorem 5.1.21 in [42]. □

By composition of continuously differentiable functions, it may be realised that $\mathbf{M} \in C^1(\mathbb{R}^2; \mathbf{Sym}_2(\mathbb{R}))$ implies $\tilde{\mathbf{\Sigma}} \in C^1([-a, a] \times [0, S]; \mathbf{M}_2(\mathbb{R}))$ and $\tilde{\mathbf{h}} \in C^1([-a, a] \times [0, S]; \mathbb{R}^2)$ for all $\bar{\mathbf{v}} \in C^1([-a, a] \times [0, S]; \mathbb{R}^2)$ and $V_r \in C^1([0, S]; [V_{\min}, V_{\max}])$. Essentially, the PDE (26) with $\varepsilon \in \mathbb{R}_{>0}$ admits regular solutions for sufficiently smooth slip inputs and rolling velocities.

3.2 Stability and passivity

Stability and passivity are two fundamental mathematical properties of the PDE (26). The former ensures that both the tyre deformations and the resulting forces and moments remain bounded in time (or, equivalently, with respect to the travelled distance), whilst the latter guarantees that energy is dissipated through frictional rolling contact. Both properties can be analysed by introducing the following Lyapunov function, which represents the total elastic energy stored in the tyre:

$$\begin{aligned} W(\mathbf{u}(\cdot, s)) &= \frac{1}{2} \int_{-a}^a \left(\mathbf{u}^T(x, s) \mathbf{K} \mathbf{u}(x, s) + \frac{\partial \mathbf{u}^T(x, s)}{\partial x} \mathbf{S} \frac{\partial \mathbf{u}(x, s)}{\partial x} \right) dx \\ &\quad + \frac{1}{2} \mathbf{u}^T(a, s) \mathbf{S} \mathbf{\Lambda}^{-1} \mathbf{u}(a, s) + \frac{1}{2} \mathbf{u}^T(-a, s) \mathbf{S} \mathbf{\Lambda}^{-1} \mathbf{u}(-a, s). \end{aligned} \quad (28)$$

For regular solutions, as those considered in Theorem 3.1, it follows from Sobolev embedding in one dimension that $\|\mathbf{u}(a, s)\|_2, \|\mathbf{u}(-a, s)\|_2 \leq C \|\mathbf{u}(\cdot, s)\|_{H^1((-a, a); \mathbb{R}^2)}$ for some $C \in \mathbb{R}_{>0}$, and therefore the

above Lyapunov function is equivalent to a squared norm on $H_1((-a, a); \mathbb{R}^2)$, and is also differentiable in the classical sense. Accordingly, taking the derivative of Eq. (28) along the dynamics (26) gives

$$\begin{aligned} \frac{dW(s)}{ds} &= \int_{-a}^a \left(\mathbf{K}\mathbf{u}(x, s) - \mathbf{S} \frac{\partial^2 \mathbf{u}(x, s)}{\partial x^2} \right)^T \frac{\partial \mathbf{u}(x, s)}{\partial s} dx + \left(\frac{\partial \mathbf{u}(a, s)}{\partial x} + \mathbf{\Lambda}^{-1} \mathbf{u}(a, s) \right)^T \mathbf{S} \frac{d\mathbf{u}(a, s)}{ds} \\ &\quad + \left(\frac{\partial \mathbf{u}(-a, s)}{\partial x} - \mathbf{\Lambda}^{-1} \mathbf{u}(-a, s) \right)^T \mathbf{S} \frac{d\mathbf{u}(-a, s)}{ds}, \quad s \in (0, S). \end{aligned} \quad (29)$$

Enforcing the BCs (26b) and (26c) and substituting Eq. (20a) into (29) yields

$$\begin{aligned} \frac{dW(s)}{ds} &= -\langle \mathbf{q}(\cdot, s), \bar{\mathbf{v}}(\cdot, s) \rangle_{L^2((-a, a); \mathbb{R}^2)} \\ &\quad + \int_{-a}^a \left(\mathbf{K}\mathbf{u}(x, s) - \mathbf{S} \frac{\partial^2 \mathbf{u}(x, s)}{\partial x^2} \right)^T \frac{\Psi(\bar{\mathbf{v}}(x, s), s)}{p(x)} \left(\mathbf{K}\mathbf{u}(x, s) - \mathbf{S} \frac{\partial^2 \mathbf{u}(x, s)}{\partial x^2} \right) dx \\ &\quad + \int_{-a}^a \left(\mathbf{K}\mathbf{u}(x, s) - \mathbf{S} \frac{\partial^2 \mathbf{u}(x, s)}{\partial x^2} \right)^T \frac{\partial \mathbf{u}(x, s)}{\partial x} dx, \quad s \in (0, S). \end{aligned} \quad (30)$$

Integrating by parts the last term appearing in Eq. (30) gives

$$\begin{aligned} \int_{-a}^a \left(\mathbf{K}\mathbf{u}(x, s) - \mathbf{S} \frac{\partial^2 \mathbf{u}(x, s)}{\partial x^2} \right)^T \frac{\partial \mathbf{u}(x, s)}{\partial x} dx &= \frac{1}{2} \mathbf{u}^T(a, s) \mathbf{K}\mathbf{u}(a, s) - \frac{1}{2} \frac{\partial \mathbf{u}^T(a, s)}{\partial x} \mathbf{S} \frac{\partial \mathbf{u}(a, s)}{\partial x} \\ &\quad - \frac{1}{2} \mathbf{u}^T(-a, s) \mathbf{K}\mathbf{u}(-a, s) + \frac{1}{2} \frac{\partial \mathbf{u}^T(-a, s)}{\partial x} \mathbf{S} \frac{\partial \mathbf{u}(-a, s)}{\partial x}, \end{aligned} \quad (31)$$

and imposing again the BCs (26b) and (26c), Eq. (30) simplifies to

$$\begin{aligned} \frac{dW(s)}{ds} &= -\langle \mathbf{q}(\cdot, s), \bar{\mathbf{v}}(\cdot, s) \rangle_{L^2((-a, a); \mathbb{R}^2)} \\ &\quad + \int_{-a}^a \left(\mathbf{K}\mathbf{u}(x, s) - \mathbf{S} \frac{\partial^2 \mathbf{u}(x, s)}{\partial x^2} \right)^T \frac{\Psi(\bar{\mathbf{v}}(x, s), s)}{p(x)} \left(\mathbf{K}\mathbf{u}(x, s) - \mathbf{S} \frac{\partial^2 \mathbf{u}(x, s)}{\partial x^2} \right) dx, \quad s \in (0, S). \end{aligned} \quad (32)$$

The inequality (32) will be instrumental in proving stability and passivity properties for the FrSD model. The next Sect. 3.2.1 focuses specifically on stability.

3.2.1 Stability

In the following, stability is analysed in terms of both state and input-to-output behaviour of the PDE (26), by adopting the notions of *input-to-state* and *input-to-output* stability. The former characterises the boundedness of the distributed states, and thus of the tyre deformations, whereas the latter concerns the boundedness of the generated forces and moment. In this context, the first theoretical result is formalised in Lemma 3.1.

Lemma 3.1 (Input-to-state stability (ISS)). *For all inputs $\bar{\mathbf{v}} \in C^1(\mathcal{C} \times \mathbb{R}_{\geq 0}; \mathbb{R}^2) \cap L^\infty([-a, a] \times \mathbb{R}_{\geq 0}; \mathbb{R}^2)$, rolling speeds $V_r \in C^1(\mathbb{R}_{\geq 0}; [V_{\min}, V_{\max}])$, and ICs $\mathbf{u}_0 \in C^{2+\alpha}([-a, a]; \mathbb{R}^2)$, $\alpha \in (0, 1)$, satisfying the BCs (26b) and (26c), the PDE (26) is (uniformly) input-to-state stable (ISS) in the spatial H^1 -norm. In particular, there exist functions $\beta \in \mathcal{KL}$ and $\gamma \in \mathcal{K}_\infty$ such that*

$$\|\mathbf{u}(\cdot, s)\|_{H^1((-a, a); \mathbb{R}^2)} \leq \beta\left(\|\mathbf{u}_0(\cdot)\|_{H^1((-a, a); \mathbb{R}^2)}, s\right) + \gamma\left(\|\bar{\mathbf{v}}(\cdot, \cdot)\|_\infty\right), \quad s \in \mathbb{R}_{\geq 0}. \quad (33)$$

Proof. Integrating by parts, it may be easily inferred that

$$\begin{aligned} \|\mathbf{q}(\cdot, s)\|_{L^2((-a, a); \mathbb{R}^2)}^2 &= \int_{-a}^a \left(\mathbf{K}\mathbf{u}(x, s) - \mathbf{S} \frac{\partial^2 \mathbf{u}(x, s)}{\partial x^2} \right)^T \left(\mathbf{K}\mathbf{u}(x, s) - \mathbf{S} \frac{\partial^2 \mathbf{u}(x, s)}{\partial x^2} \right) dx \\ &\geq \int_{-a}^a \left(\mathbf{u}^T(x, s) \mathbf{K}^2 \mathbf{u}(x, s) + 2 \frac{\partial \mathbf{u}^T(x, s)}{\partial x} \mathbf{K} \mathbf{S} \frac{\partial \mathbf{u}(x, s)}{\partial x} + \frac{\partial^2 \mathbf{u}^T(x, s)}{\partial x^2} \mathbf{S}^2 \frac{\partial^2 \mathbf{u}(x, s)}{\partial x^2} \right) dx \\ &\geq \gamma_0 \|\mathbf{u}(\cdot, s)\|_{H^1((-a, a); \mathbb{R}^2)}^2, \end{aligned} \quad (34)$$

for some $\gamma_0 \in \mathbb{R}_{>0}$. Moreover, $\varepsilon \in \mathbb{R}_{>0}$ implies the existence of $\gamma_1 \in \mathbb{R}_{>0}$ such that

$$\int_{-a}^a \left(\mathbf{K}\mathbf{u}(x, s) - \mathbf{S} \frac{\partial^2 \mathbf{u}(x, s)}{\partial x^2} \right)^\top \frac{\Psi(\bar{\mathbf{v}}(x, s), s)}{p(x)} \left(\mathbf{K}\mathbf{u}(x, s) - \mathbf{S} \frac{\partial^2 \mathbf{u}(x, s)}{\partial x^2} \right) dx \leq \gamma_1 \|\mathbf{q}(\cdot, s)\|_{L^2((-a, a); \mathbb{R}^2)}^2. \quad (35)$$

Consequently, applying Cauchy-Schwarz and then the generalised Young's inequality for product to the first term in Eq. (32) yields

$$\frac{dW(s)}{ds} \leq -\frac{\gamma_1}{2} \|\mathbf{q}(\cdot, s)\|_{L^2((-a, a); \mathbb{R}^2)}^2 + \frac{1}{2\gamma_1} \|\bar{\mathbf{v}}(\cdot, s)\|_{L^2((-a, a); \mathbb{R}^2)}^2, \quad s \in \mathbb{R}_{>0}. \quad (36)$$

Recalling Eq. (34), it may be concluded that there exist $\rho, \mu \in \mathbb{R}_{>0}$ such that

$$\frac{dW(s)}{ds} \leq -\rho W(s) + \mu \|\bar{\mathbf{v}}(\cdot, \cdot)\|_\infty^2, \quad s \in \mathbb{R}_{>0}. \quad (37)$$

Finally, invoking the Grönwall-Bellman inequality provides

$$W(\mathbf{u}(\cdot, s)) \leq \exp(-\rho s) W(\mathbf{u}_0(\cdot)) + \frac{\mu}{\rho} \|\bar{\mathbf{v}}(\cdot, \cdot)\|_\infty^2, \quad s \in \mathbb{R}_{\geq 0}. \quad (38)$$

Since the Lyapunov function (28) is equivalent to a squared norm on $H^1((-a, a); \mathbb{R}^2)$, Eq. (38) implies (33). \square

Lemma 3.1 is concerned with the ISS behaviour of the PDE (26), and asserts boundedness for the distributed state $\mathbf{u}(x, s)$ in the spatial H^1 -norm. Combining this result with Eq. (24), it is possible to deduce the existence of $\beta_1, \beta_2, \beta_3 \in \mathbb{R}_{>0}$ such that

$$\|\mathbf{F}_x(s)\|_2 \leq \beta_1 \|\mathbf{u}(\cdot, s)\|_{H^1((-a, a); \mathbb{R}^2)}, \quad (39a)$$

$$|M_z(s)| \leq \beta_2 \|\mathbf{u}(\cdot, s)\|_{H^1((-a, a); \mathbb{R}^2)} + \beta_3 \|\mathbf{u}(\cdot, s)\|_{H^1((-a, a); \mathbb{R}^2)}^2, \quad s \in \mathbb{R}_{\geq 0}. \quad (39b)$$

The bounds derived in Eq. (39) immediately imply IOS for the tyre forces and aligning moment, according to Corollary 3.1 below.

Corollary 3.1 (Input-to-output stability (IOS)). *Under the same assumptions as Lemma 3.1, the PDE (26) with output (24) is input-to-output stable (IOS).*

Corollary 3.1 concludes the stability analysis of the FrSD model. Before moving to Sect. 3.2.2, an additional remark is collected below.

Remark 3.1. *Stability was proved by explicitly exploiting the presence of the regularisation parameter $\varepsilon \in \mathbb{R}_{>0}$ in the diffusive term. This choice was motivated by the observation that its introduction appears to be an indispensable requirement for preserving the parabolic character of Eq. (20) for all slip and spin inputs. Nevertheless, it is worth noting that alternative notions of stability can be proved without relying on its presence. For instance, in the case of a spatially invariant rigid slip velocity (i.e., in the absence of spin), boundedness can be established using exactly the same arguments as those in [43].*

3.2.2 Dissipativity and passivity

Being primarily governed by friction, tyre-road interactions dissipate energy. Concerning the string-like tyre model detailed in Sect. 2.1.1, this is obviously true when sliding occurs, and the nondimensional friction force assumes the form (8). However, since the FrSD model described by Eqs. (20) and (23) is merely an approximation to the true string-like tyre dynamics, it is interesting to investigate whether the dissipative properties of the rolling process are preserved after applying Theorem 2.1. In particular, recalling Eq. (3) and computing the dissipation rate gives

$$\begin{aligned} \langle \mathbf{q}(\cdot, s), \mathbf{v}_s(\cdot, s) \rangle_{L^2((-a, a); \mathbb{R}^2)} &= - \int_{-a}^a \mathbf{q}^\top(x, s) \mathbf{v}_s(x, s) dx \\ &= - \int_{-a}^a V_r(s) \mathbf{q}^\top(x, s) \frac{\Psi(\bar{\mathbf{v}}_r(x, s), s)}{p(x)} \mathbf{q}(x, s) dx \geq 0, \quad s \in [0, S], \end{aligned} \quad (40)$$

which confirms that the FrSD model still predicts energy dissipation within the tyre's contact patch. The inequality derived according to Eq. (40) employs the actual sliding velocity of the tyre particles, and pertains to the physical nature of the rolling contact process. From a dynamical system theory perspective, however, it is also meaningful to study the passivity properties of the FrSD model when the nondimensional rigid slip velocity $\bar{\mathbf{v}}(x, s)$ is regarded as the input to the PDE (26) with output (24a). In this context, passivity results are formalised in Lemma 3.2 below.

Lemma 3.2 (Passivity). *For all inputs $\bar{\mathbf{v}} \in C^1([-a, a] \times \mathbb{R}_{\geq 0}; \mathbb{R}^2) \cap L^\infty(\mathcal{C} \times \mathbb{R}_{\geq 0}; \mathbb{R}^2)$, rolling speeds $V_r \in [V_{\min}, V_{\max}]$, and ICs $\mathbf{u}_0 \in C^{2+\alpha}([-a, a]; \mathbb{R}^2)$, $\alpha \in (0, 1)$, satisfying the BCs (26b) and (26c), the system described by the PDE (26) with output (24a) is passive. In particular,*

$$-\int_0^s \langle \mathbf{q}(\cdot, s'), \bar{\mathbf{v}}(\cdot, s') \rangle_{L^2((-a, a); \mathbb{R}^2)} ds' \geq W(\mathbf{u}(\cdot, s)) - W(\mathbf{u}_0(\cdot)), \quad s \in [0, S], \quad (41)$$

with storage function $W(\mathbf{u}(\cdot, s))$ as in Eq. (28).

Proof. Since the second term on the right-hand side of Eq. (32) is negative definite, it holds that

$$-\langle \mathbf{q}(\cdot, s), \bar{\mathbf{v}}(\cdot, s) \rangle_{L^2((-a, a); \mathbb{R}^2)} \geq \frac{dW(\mathbf{u}(\cdot, s))}{ds}, \quad s \in (0, S). \quad (42)$$

Integrating the above (42) yields the result. \square

Combining Eqs. (32) and (40), it may also be concluded that

$$-\langle \mathbf{q}(\cdot, s), \mathbf{v}(\cdot, s) \rangle_{L^2((-a, a); \mathbb{R}^2)} = -\langle \mathbf{q}(\cdot, s), \mathbf{v}_s(\cdot, s) \rangle_{L^2((-a, a); \mathbb{R}^2)} + V_r(s) \frac{dW(\mathbf{u}(\cdot, s))}{ds}, \quad s \in [0, S], \quad (43)$$

which establishes that the difference between the energy dissipation rates associated with the sliding and rigid slip velocities is precisely equal to the elastic energy stored in the tyre system. In line with the findings of [44], this further implies that slip losses cannot, in general, be evaluated as the inner product of the global tyre forces and moment with the corresponding slip and spin inputs, with the equivalence being only recovered in steady-state conditions [45–47].

4 Numerical and experimental validation

The FrSD tyre model developed in Sect. 2.2 is validated numerically and experimentally in Sects. 4.1 and 4.2.

4.1 Numerical simulations

In the following, simulation results are reported to illustrate both the stationary and transient behaviours of the tyre predicted using the FrSD model. Specifically, Sect. 4.1.1 is dedicated to the qualitative analysis of the steady-state tyre forces and moments, whereas the dynamic features of the new formulation are discussed in Sect. 4.1.2.

4.1.1 Steady-state behaviour

A first set of numerical results is presented to elucidate the steady-state behavior of the FrSD tyre model developed in Sect. 2.2. Figure 1 shows the lateral deflection $u_y(x)$, lateral stress $q_y(x)$, and longitudinal stress $q_x(x)$ for a translational slip input $\boldsymbol{\sigma} = (0.2, 0.2)$, considering two model parametrisations (P1 and P2) with parameters listed in Table 1 and taken from [20].

Specifically, Fig. 1(a), corresponding to P1 in Table 1, highlights the portions of the string in contact with the road (shaded blue) and the free segments of the tyre (shaded green). Consistent with the model assumptions and imposed boundary conditions, the lateral deflection $u_y(x)$ decays exponentially for $x \in (-\infty, -a] \cup [a, \infty)$, whilst displaying an almost parabolic profile within the contact region $x \in [-a, a]$. Notably, no kink appears at the trailing edge, in agreement with the discussion initiated in Sect. 2.2.1. Both the longitudinal and lateral stresses vanish outside the contact zone and grow nonlinearly from the leading to the trailing edge. In particular, the longitudinal stresses reach higher magnitudes than lateral ones, reflecting the tyre's greater stiffness along the longitudinal direction. Analogous observations apply to the trends illustrated in Fig. 1(b), produced employing smaller values for the relaxation lengths (P2

Table 1: Model parameters

Parameter	Description	Unit	Value (P1)	Value (P2)
k_x	Longitudinal stiffness	N m ²	$2 \cdot 10^5$	$6 \cdot 10^5$
k_y	Lateral stiffness	N m ²	$1 \cdot 10^5$	$3 \cdot 10^5$
λ_x	Longitudinal relaxation length	m	0.3	0.1
λ_y	Lateral relaxation length	m	0.5	0.2
EA	Bending stiffness	N	$1.8 \cdot 10^4$	$6 \cdot 10^3$
S	Effective string tension	N	$2.5 \cdot 10^4$	$1.2 \cdot 10^4$
a	Contact patch semilength	m	0.05	0.05
V_r	Rolling speed	m s ⁻¹	16	16
μ_s	Static friction coefficient	-	1	1
μ_d	Dynamic friction coefficient	-	0.7	0.7
v_S	Stribeck velocity	m s ⁻¹	3.49	3.49
δ_S	Stribeck exponent	-	0.6	0.6
F_z	Vertical force	N	3000	3000
ε	Regularisation parameter	-	$1 \cdot 10^{-12}$	$1 \cdot 10^{-12}$

in Table 1). The predicted behavior is qualitatively consistent with that reported in [20], with the main difference being that the shear stresses remain continuous along the contact length.

Figures 2 and 3 illustrate the main tyre characteristics produced employing parametrisations P1 and P2, respectively, and considering different combinations of translational slip inputs and a constant pressure distribution. In agreement with classical results from Coulomb-type friction models, the lateral tyre force F_y and the aligning moment M_z exhibit a peak whose magnitude decreases under combined slip conditions. Both quantities approach asymptotic values at large σ_y . Although not explicitly shown in Figs. 2 and 3, the sign reversal phenomenon typically observed in the aligning moment can be reproduced using asymmetric pressure distributions, for example, a slowly decaying exponential along the contact length. Inspection of the friction ellipses in Figs. 2 and 3 indicate that, despite the applied normal load of $F_z = 3$ kN, the total tangential force does not exceed 2.5 kN at very large slips. This behaviour is a direct consequence of the adopted friction model, in which the dynamic coefficient is significantly lower than the static one (Table 1). Finally, particularly noteworthy is the trend of the aligning moment versus the longitudinal force. Large slip values induce significant carcass deflections, producing asymmetries in the vertical moment, as evident in both figures. In particular, negative longitudinal forces lead to a sign reversal, in agreement with the predictions of [20].

4.1.2 Transient behaviour

Compared with the model variants introduced in [38, 39], which rely on local rheological descriptions of the carcass and tread deflections, the proposed FrSD model can capture relaxation phenomena more accurately owing to the diffusive properties of Eq. (20a), which are inherited from the nonlocal constitutive equation (1). This feature permits accounting for nonlinear unsteady responses excited by large slip inputs, which generate short-lived transients. In this context, Fig. 4 depicts the evolution of the lateral tyre force and aligning moment following step changes in slip of varying magnitude. Inspection of Fig. 4 shows that increasing slip levels lead to faster relaxation dynamics. This behavior persists even for slip inputs exceeding those associated with the peak values of the tyre characteristics, as evidenced, for instance, by the responses of both F_y and M_z for $\sigma_y = 0.2$.

A further distinctive capability of the FrSD model is its tendency to mitigate or suppress oscillations induced by time-varying slip inputs. This effect is illustrated in Fig. 5, where the tyre is subjected to a sinusoidal input of the form $\sigma_y(s) = \bar{\sigma}_y[1 + 0.5 \sin(\omega s)]$, with $\omega = 5$ m⁻¹. Particularly at large values of $\bar{\sigma}_y$, the system exhibits a pronounced low-pass filtering behaviour. From a mathematical standpoint, this property originates again from the nonlinear diffusive term in Eq. (20a). Near saturation, fluctuations around the steady-state lateral force are further reduced due to the high friction utilisation. For a fixed value of $\bar{\sigma}_y$, higher-frequency oscillations in the slip input are increasingly attenuated. This trend is evident in Fig. 6, which shows the transient responses of the lateral force and vertical moment for $\bar{\sigma}_y = 0.08$ and $\omega = 5, 10, \text{ and } 20$ m⁻¹.

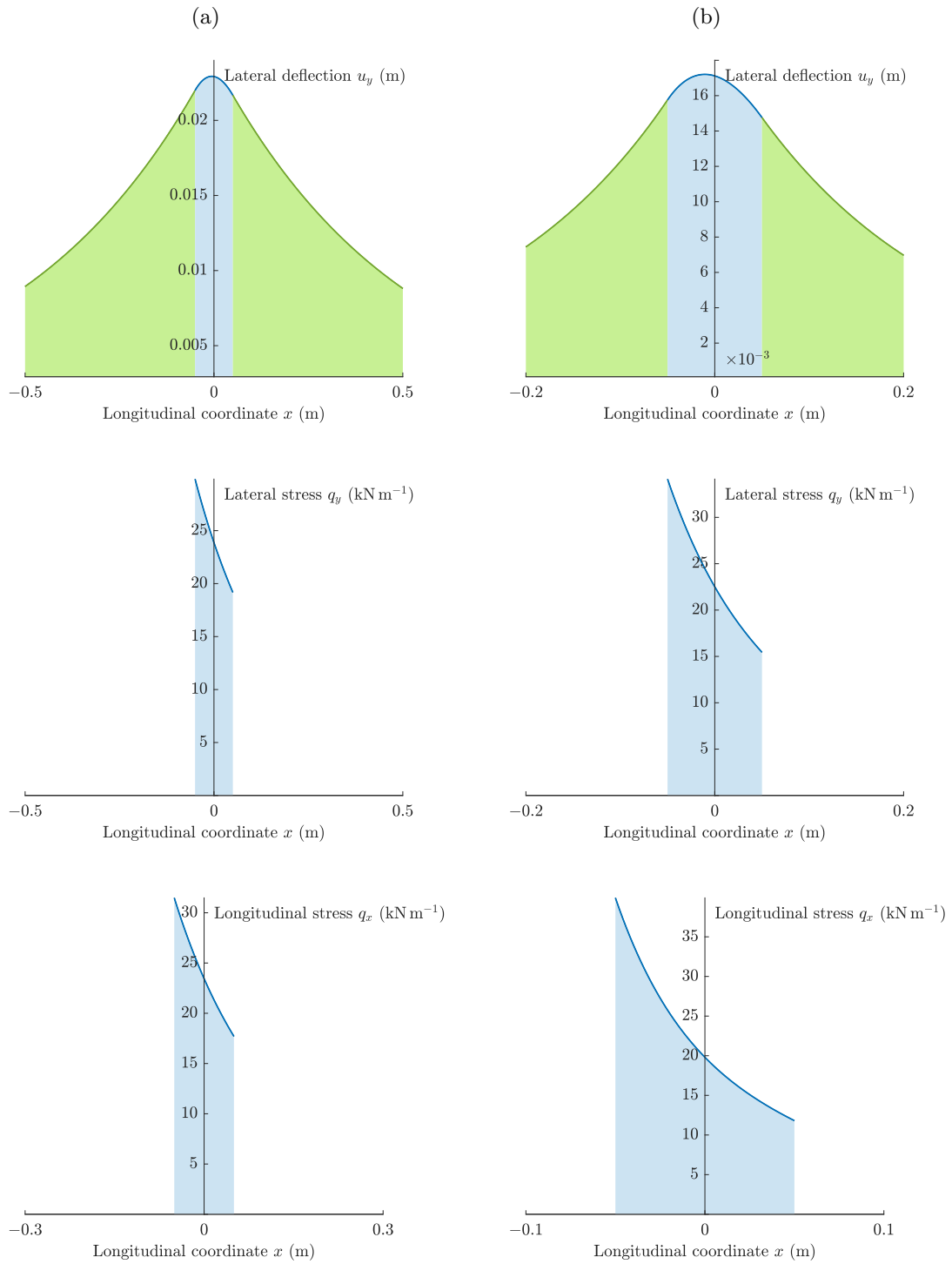


Figure 1: Steady-state lateral deflection and shear stresses. Model parameters as in Table 1: (a) P1; (b) P2.

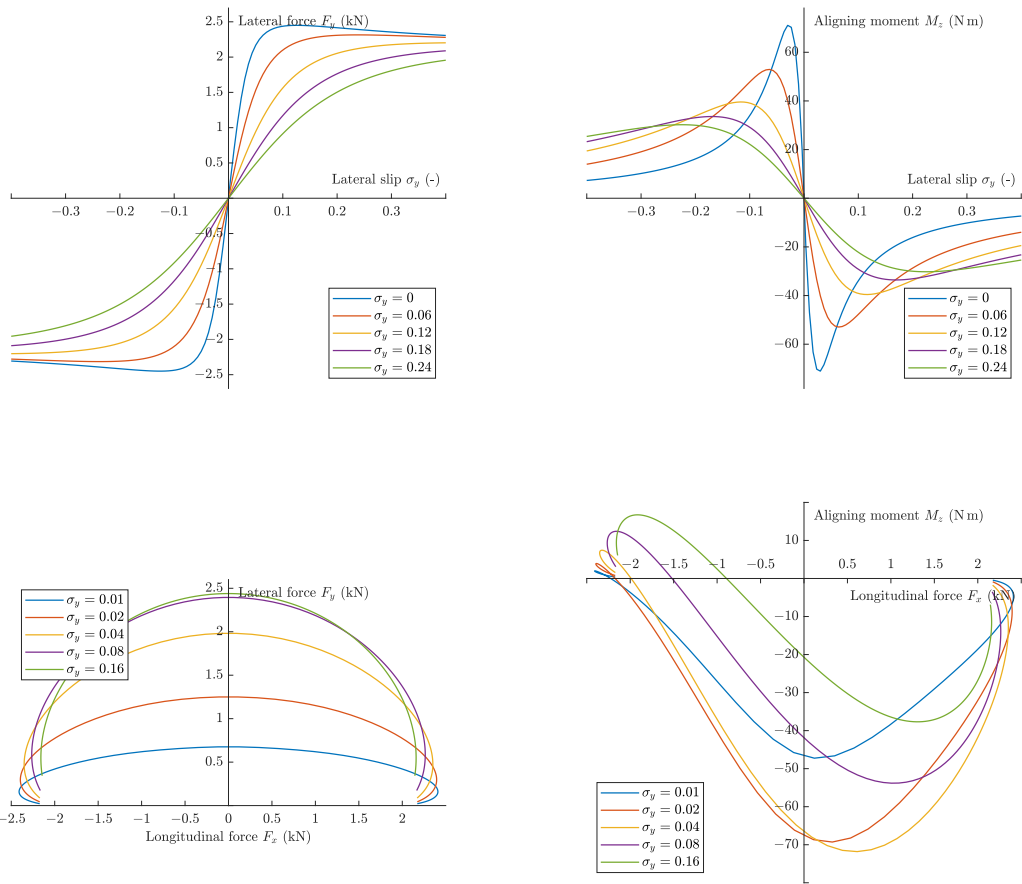


Figure 2: Steady-state tyre characteristics. Model parameters as in Table 1 (P1).

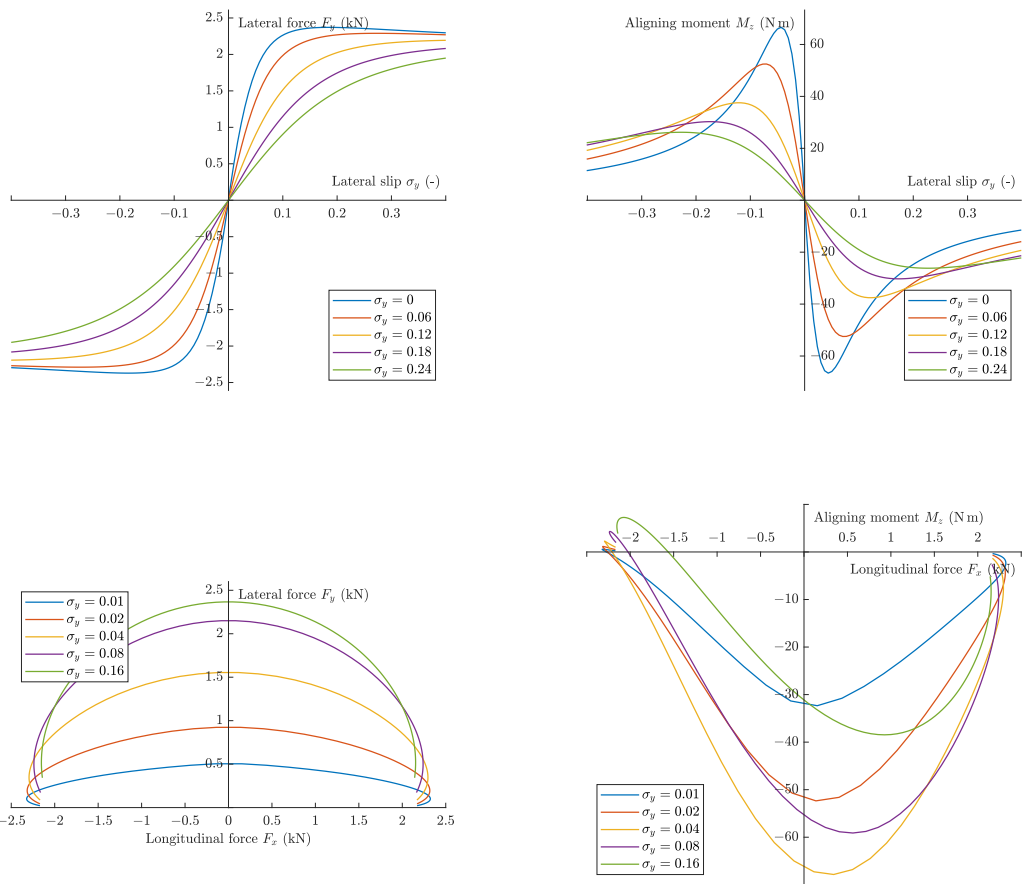


Figure 3: Steady-state tyre characteristics. Model parameters as in Table 1 (P2).

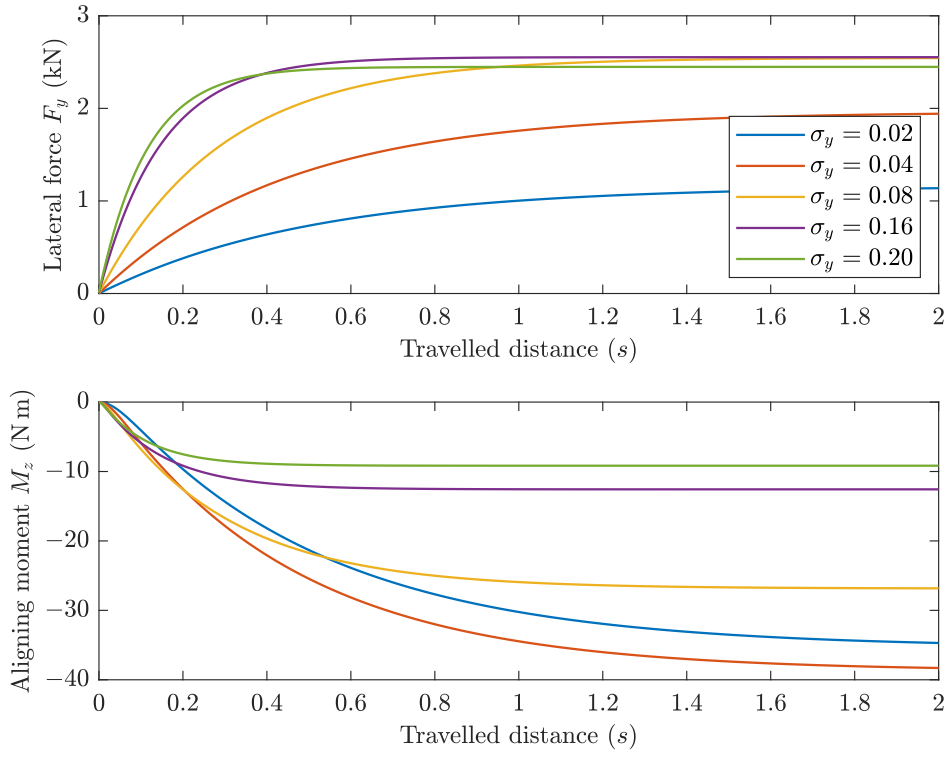


Figure 4: Transient response to different step slip inputs. Model parameters as in Table 1.

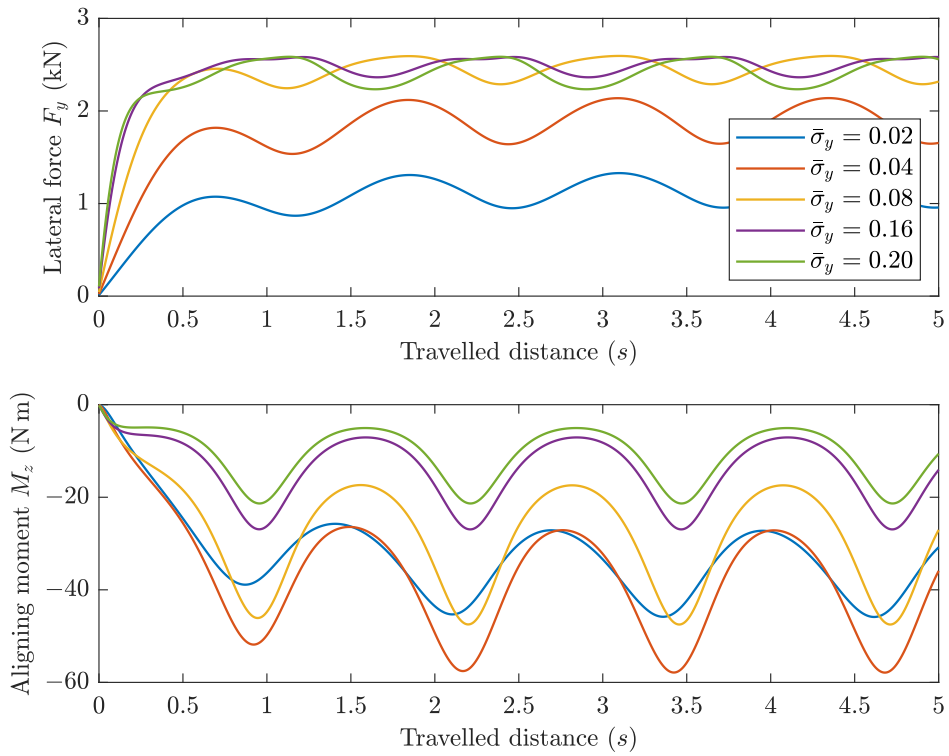


Figure 5: Transient lateral response to a sinusoidal slip input $\sigma_y(s) = \bar{\sigma}_y[1 + 0.5 \sin(\omega s)]$ for different values of $\bar{\sigma}_y$ and $\omega = 5 \text{ m}^{-1}$. Model parameters as in Table 1.

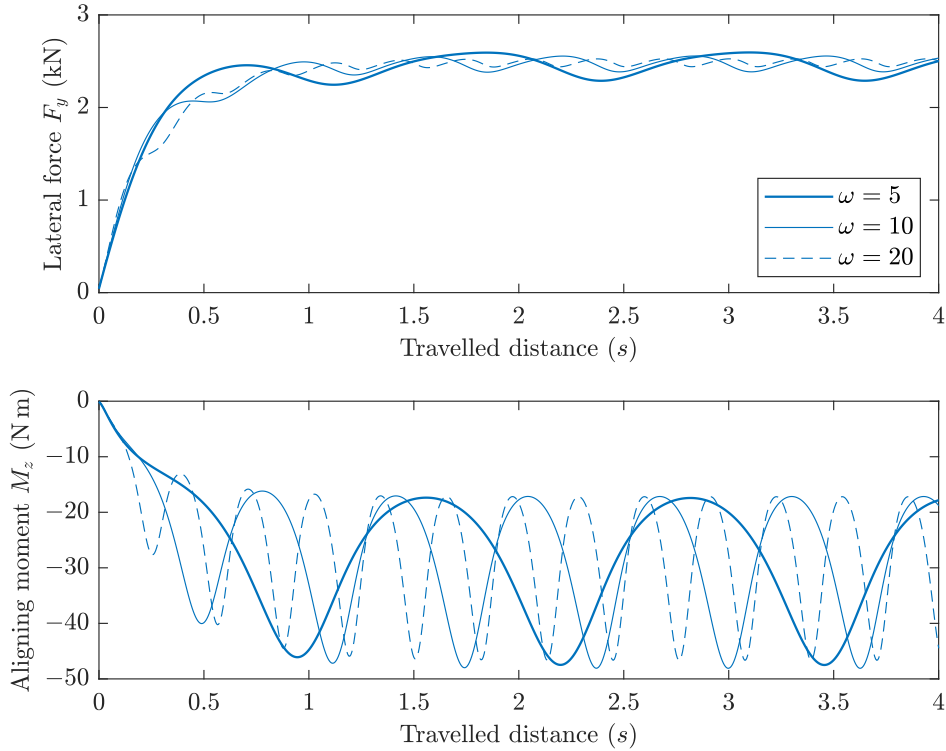


Figure 6: Transient lateral response to a sinusoidal slip input $\sigma_y(s) = \bar{\sigma}_y[1 + 0.5 \sin(\omega s)]$ for $\bar{\sigma}_y = 0.08$ and different values of ω . Model parameters as in Table 1.

4.2 Experimental validation

The FrSD model was validated against data collected from a test rig [40, 48, 49]. The next Sects. 4.2.1 and 4.2.2 present experimental results concerning the lateral tyre deflection and transient response to step slip inputs, respectively.

4.2.1 Steady-state tyre carcass deflection

The carcass and sidewall elements may undergo relatively large deformations when a tyre is subjected to lateral slip, i.e., to a sideslip angle ($\tan \alpha = \sigma_y$ in the absence of longitudinal slip). For the purpose of model validation, the tyre deflection was measured with high accuracy using optical devices, specifically the setup described in [40, 48, 49]. Figure 7 compares the experimentally measured lateral deformations to the steady-state response predicted by the FrSD model (dashed lines), for several values of the sideslip angle. In the vicinity of the contact patch ($|\theta| < 10^\circ$), the FrSD model qualitatively reproduces both the magnitude and the profile of the measured deformation. For larger values of $|\theta|$, the approximation introduced by assuming exponentially decaying functions for $|x| > a$ results in noticeable deviations. Nevertheless, the agreement outside the contact patch is of limited relevance for the evaluation of tyre forces and moments, since, according to Eq. (24), these quantities can be determined solely from the deflection profile within the contact patch and the boundary conditions at the leading and trailing edges.

The deformation trends illustrated in Fig. 7 were obtained by calibrating the FrSD model parameters using a genetic algorithm implemented in MATLAB[®]. The identified parameters, listed in Table 2, were optimised to reproduce the experimental deformation profiles over the angular range $\theta \in [135^\circ, 225^\circ]$, in accordance with the observations reported above.

4.2.2 Relaxation behaviour

The relaxation behaviour of the tyre was investigated experimentally by analysing the transient response to practical longitudinal step slip inputs κ_x ($\sigma_x = \frac{\kappa_x}{1+\kappa_x}$ in the absence of lateral slip). Figure 8 compares

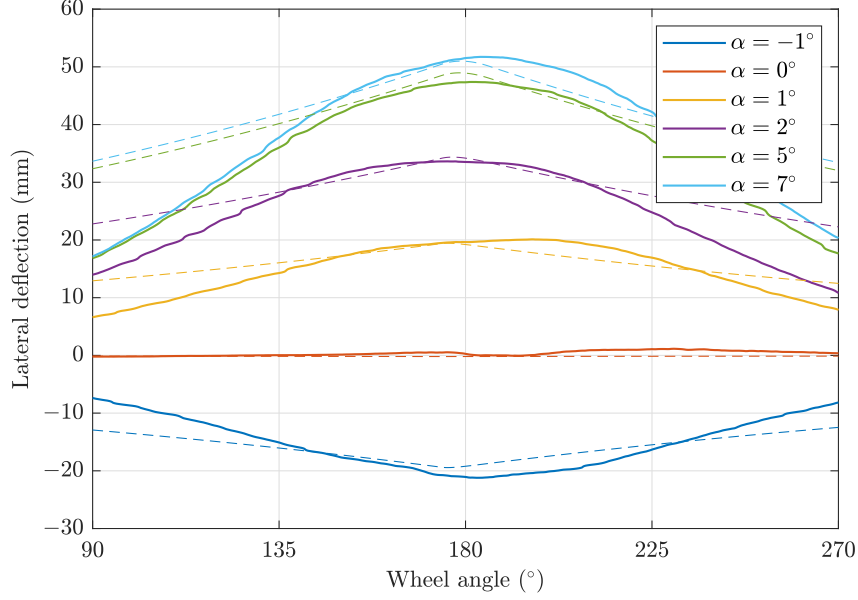


Figure 7: Steady-state lateral carcass deflection for different tyre sideslip angles. Line styles: Experimental (thick solid lines), FrSD model (dashed lines). Model parameters as in Table 2.

Table 2: Model parameters

Parameter	Description	Unit	Value
k_y	Lateral stiffness	N m^2	$3.00 \cdot 10^4$
λ_y	Lateral relaxation length	m	1.089
a	Contact patch semilength	m	0.03
μ_s	Static friction coefficient	-	1.03
μ_d	Dynamic friction coefficient	-	0.72
v_S	Stribeck velocity	m s^{-1}	10
δ_S	Stribeck exponent	-	2
F_z	Vertical force	N	3700
ε	Regularisation parameter	-	$1 \cdot 10^{-12}$

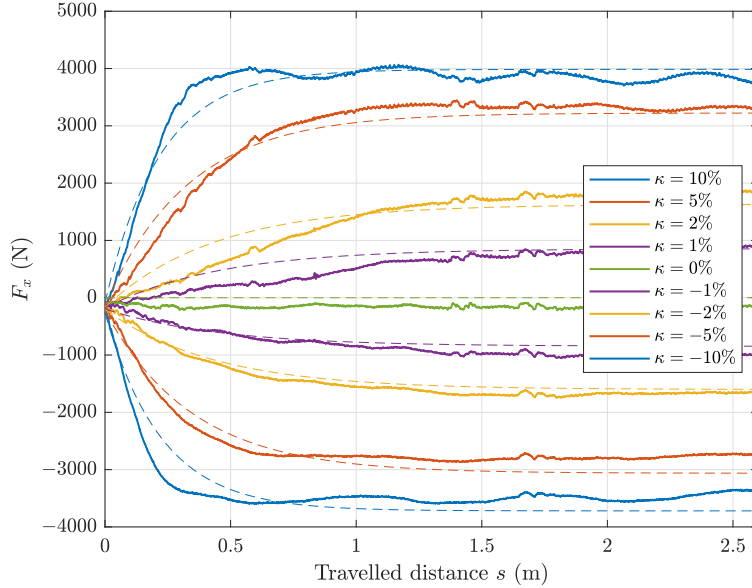


Figure 8: Longitudinal relaxation behaviour of the tyre subjected to different practical step slip inputs. Line styles: Experimental (thick solid lines), FrSD model (dashed lines). Model parameters as in Table 3.

Table 3: Model parameters

Parameter	Description	Unit	Value
k_x	Longitudinal stiffness	N m^2	$1.68 \cdot 10^5$
λ_x	Longitudinal relaxation length	m	0.51
a	Contact patch semilength	m	0.05
μ_s	Static friction coefficient	-	0.83
μ_d	Dynamic friction coefficient	-	0.58
v_S	Stribeck velocity	m s^{-1}	1.07
δ_S	Stribeck exponent	-	2
F_z	Vertical force	N	3700
ε	Regularisation parameter	-	$1 \cdot 10^{-12}$

the experimental data with the predictions of the FrSD model, whose parameters (listed in Table 3) were optimised using a genetic algorithm implemented in MATLAB/Simulink[®].

Inspection of Fig. 8 indicates that the FrSD model captures the nonlinear relaxation effects with satisfactory accuracy across the entire range of slip inputs, correctly predicting convergence to the true steady-state longitudinal force. This also confirms the model’s ability to reproduce the stationary tyre characteristic over a wide range of slip values. Some discrepancies are nevertheless observed concerning the transient behaviour at larger slip values, where the optimised model exhibits slower transient dynamics. It is also worth noting that the response is not symmetric with respect to the slip input, with the FrSD description slightly overestimating the magnitude of the steady-state longitudinal force for $\kappa_x = -0.1$ and $\kappa_x = -0.05$.

5 Conclusions

This paper presented a new string-like tyre model with distributed friction dynamics, renamed FrSD (*friction with string dynamics*). By combining a nonlocal constitutive representation of the tyre structural deformation with a dynamic friction law of FrBD type, the proposed formulation departs from classical transport-dominated rolling contact models and leads to a system of semilinear parabolic partial differential equations.

A central outcome of this work is the recognition that the inclusion of higher-order spatial derivatives

in the constitutive tyre equations fundamentally alters the mathematical character of the rolling contact process. In contrast to traditional hyperbolic formulations, the parabolic structure of the FrSD model naturally introduces diffusive effects that govern the evolution of the treadband and carcass deflections within the contact patch. These mechanisms provide a physically consistent explanation for relaxation phenomena that depend on slip and spin magnitude, as well as for the observed attenuation of high-frequency slip excitations. The proposed formulation retains the key advantages of the string and brush tyre models – including physical interpretability and a clear link between local deformation and global force generation – whilst addressing several of their well-known limitations. In particular, the ability to impose boundary conditions at both ends of the contact patch yields smooth deformation profiles, avoiding artificial discontinuities at the leading or trailing edge. Moreover, the regularised FrBD friction law ensures well-posedness and numerical robustness across the full range of operating conditions.

Numerical simulations demonstrated that the FrSD model reproduces classical steady-state tyre characteristics under combined slip conditions, including force saturation and aligning moment behaviour. At the same time, it captures distinctive transient features such as slip-dependent relaxation speeds and a pronounced low-pass filtering of oscillatory inputs. These properties are particularly relevant for vehicle dynamics simulations involving aggressive manoeuvres, stability control, and high-bandwidth actuation.

From a vehicle systems perspective, the proposed formulation provides a promising basis for the development of tyre models that are both physically grounded and suitable for integration into control-oriented and multibody simulation frameworks. The parabolic structure facilitates theoretical analysis, including stability and dissipativity studies, and may prove advantageous in the context of reduced-order modelling and real-time applications. Future work will focus on extensions to account for additional physical effects such as camber, pressure variations, and viscoelastic tread behaviour. The series connection between string-like and bristle elements should also be implemented to improve the relaxation behaviour of the tyre model. Further investigation of the implications of the parabolic structure for vehicle-level stability and control design also represents a promising direction for ongoing research.

Funding declaration

This research was financially supported by the project FASTEST (Reg. no. 2023-06511), funded by the Swedish Research Council.

Acknowledgements

The author thanks Igo Besselink at TU/e for providing the experimental data used in Sect. 4.2.

Compliance with Ethical Standards

The authors declare that they have no conflict of interest.

Author Contribution declaration

L.R. is the sole author of and contributor to the manuscript.

References

- [1] Rajamani R. Vehicle Dynamics and Control, 1st ed. Springer New York, NY (2012). Available from: <https://doi.org/10.1007/978-1-4614-1433-9>.
- [2] Kiencke U, Nielsen L. Automotive Control Systems, 2nd ed. Springer Berlin, Heidelberg (2005).
- [3] Savaresi S, Tanelli M. Active Braking Control Systems Design for Vehicles. Springer, London (2010).
- [4] Yu H, Qi Z, Duan J, Taheri S, Ma Y. Multiple model adaptive backstepping control for antilock braking system based on LuGre dynamic tyre model. International Journal of Vehicle Design. 2015;69(1-4):168-184.
- [5] Satzger C, de Castro R. Predictive Brake Control for Electric Vehicles, IEEE Transactions on Vehicular Technology 67(2):977-990 (2018).

- [6] Poussot-Vassal C, Sename O, Dugard L, et al. Attitude and handling improvements through gain-scheduled suspensions and brakes control, *Control Engineering Practice* 19(3) (2011).
- [7] Wang WY, Li IH, Chen MC, et al. Dynamic Slip-Ratio Estimation and Control of Antilock Braking Systems Using an Observer-Based Direct Adaptive Fuzzy-Neural Controller, *IEEE Transactions on Industrial Electronics* 56(5):1746-1756 (2009).
- [8] Hou X, Zhang J, Liu W, Ji Y. LuGre Model-based Longitudinal Ride Comfort Control of Vehicle during the Post-braking Phase. 2020 Chinese Automation Congress (CAC). 2020:7307-7313. Available from: <https://doi.org/110.1109/CAC51589.2020.9327063>.
- [9] Solyom S. Synthesis of a Model-Based Tire Slip Controller. *Vehicle Syst Dyn* 41(6):475-499 (2004).
- [10] de Castro R, Araújo RE, Freitas D. Wheel Slip Control of EVs Based on Sliding Mode Technique With Conditional Integrators, *IEEE Transactions on Industrial Electronics* 60(8):3256-3271 (2013).
- [11] Fors V, Olofsson B, Nielsen L. Formulation and interpretation of optimal braking and steering patterns towards autonomous safety-critical manoeuvres, *Vehicle Syst Dyn* 57(8):1206-1223 (2019). Available from: <https://doi.org/10.1080/00423114.2018.1549331>.
- [12] Fors V, Olofsson B, Nielsen L. Attainable force volumes of optimal autonomous at-the-limit vehicle manoeuvres, *Vehicle Syst Dyn* 58(7):1101-1122 (2020). Available from: <https://doi.org/10.1080/00423114.2019.1608363>.
- [13] Fors V, Olofsson B, Nielsen L. Autonomous Wary Collision Avoidance, *IEEE Transactions on Intelligent Vehicles* 6(2):353-365 (2021). Available from: <https://doi.org/10.1109/TIV.2020.3029853>.
- [14] Fors V, Anistratov P, Olofsson B, Nielsen L. Predictive Force-Centric Emergency Collision Avoidance, *ASME. J. Dyn. Sys., Meas., Control.* 143(8):081005 (2021). Available from: <https://doi.org/10.1115/1.4050403>.
- [15] Pacejka HB. *Tire and Vehicle Dynamics*. 3rd ed. Elsevier, Amsterdam (2012).
- [16] Guiggiani M. *The Science of Vehicle Dynamics*. 3rd ed. Springer, Cham (2023). Available from: <https://doi.org/10.1007/978-3-031-06461-6>.
- [17] Romano L. *Advanced Brush Tyre Modelling*. SpringerBriefs in Applied Sciences. Springer, Cham (2022). Available from: <https://doi.org/10.1007/978-3-030-98435-9>.
- [18] Schlippe B von, Dietrich R. Das flattern eined bepneuten rades. Bericht 140 der Lilienthal Gesellschaft. 1941: NACA TM 1365.
- [19] Force and moment response of pneumatic tires to lateral motion inputs. *Transaction ASME, Journal of Engineering for Industry*, 88B. 1966.
- [20] Higuchi A. *Transient response of tyres at large wheel slip and camber [doctoral thesis]*. Delft; 1997.
- [21] Higuchi A, Pacejka HB. The relaxation length concept at large wheel slip and camber. *Veh Syst Dyn* 25(sup001):50-64 (1997). Available from: <https://doi.org/10.1080/00423119708969644>.
- [22] Pauwelussen JP. The Local Contact Between Tyre and Road Under Steady State Combined Slip Conditions. *Vehicle Syst. Dyn.* 2004;41(1):1-26. Available from: <http://doi.org/10.1076/vesd.41.1.1.23406>.
- [23] Johnson KL. *Contact Mechanics*. Cambridge University Press (1985). Available from: <https://doi.org/10.1017/CB09781139171731>.
- [24] Rill G. Simple contact calculation for handling tyre models. *Multibody Syst Dyn* 45:131-153 (2019). Available from: <https://doi.org/10.1007/s11044-018-9629-4>.
- [25] Shaju A, Pandey AK. Modelling transient response using PAC 2002-based tyre model. *Veh Syst Dyn* (2020). Available from: <https://doi.org/10.1080/00423114.2020.1802048>.
- [26] Romano L, Bruzelius F, Jacobson B. Unsteady-state brush theory. *Veh Syst Dyn* (2020). Available from: <https://doi.org/10.1080/00423114.2020.1774625>.
- [27] Romano L, Timpone F, Bruzelius F, Jacobson B. Analytical results in transient brush tyre models: theory for large camber angles and classic solutions with limited friction. *Meccanica* 57:165-191 (2022). Available from: <http://dx.doi.org/10.1007/s11012-021-01422-3>.
- [28] Sorine M, Szymanski J. A new dynamic multi d.o.f. tire model. *Transportation Systems 2000*, Braunschweig (2000).
- [29] Canudas-de-Wit C, Tsiotras P. Dynamic tire friction models for vehicle traction control. *Proc. 38th IEEE CDC*, 3746-3751 (1999). Available from: <https://doi.org/10.1109/CDC.1999.827937>.
- [30] Canudas-de-Wit C, Tsiotras P, Velenis E, et al. Dynamic friction models for road/tire longitudinal interaction. *Veh Syst Dyn* 39(3):189-226 (2003). Available from: <https://doi.org/10.1076/vesd.39.3.189.14152>.
- [31] Velenis E, Tsiotras P, Canudas-de-Wit C, Sorine M. Dynamic tyre friction models for combined slip. *Veh Syst Dyn* 43:3-29 (2005). Available from: <https://doi.org/10.1080/00423110412331290464>.
- [32] Deur J. Modeling and analysis of longitudinal tire dynamics based on the LuGre friction model.

- IFAC Proc Vol 34(1):91–96 (2001). Available from: [https://doi.org/10.1016/S1474-6670\(17\)34383-5](https://doi.org/10.1016/S1474-6670(17)34383-5).
- [33] Deur J, Asgari J, Hrovat D. A 3D brush-type dynamic tire friction model. *Veh Syst Dyn* 42(3):133–173 (2004). Available from: <https://doi.org/10.1080/00423110412331282887>.
- [34] Deur J, Ivanović V, Troulis M, et al. Extensions of the LuGre tyre friction model for variable slip speed. *Veh Syst Dyn* 43(1):508–524 (2005). Available from: <https://doi.org/10.1080/00423110500229808>.
- [35] Zhang M, Unrau HJ, Gießler M, Gauterin F. Tire tread wear characteristics: insights from indoor experiments and analytical modeling. *Tribology International* 10 (2025). Available from: <https://doi.org/10.1016/j.triboint.2025.110752>.
- [36] Zhang M, Unrau HJ, Gießler M, Gauterin F. A detailed tire tread friction model considering dynamic friction states. *Tribology International* 193 (2024). Available from: <https://doi.org/10.1016/j.triboint.2024.109342>.
- [37] Romano L, Aamo OM, Åslund J, Frisk E. First-order friction models with bristle dynamics: lumped and distributed formulations. Submitted to *IEEE Trans Control Syst Technol* (2025).
- [38] Romano L. Two-dimensional FrBD friction models for rolling contact. *Nonlinear Dynamics* (2025).
- [39] Romano L. Two-dimensional FrBD friction models for rolling contact: extension to linear viscoelasticity. Submitted to *Tribology International* (2025).
- [40] Besselink IJM, Aertssen AJ, Thakkar D, Lugaro C. Measurement of tire vertical damping, carcass deflection and longitudinal relaxation length. In W. Huang, & M. Ahmadian (Eds.), *Advances in Dynamics of Vehicles on Roads and Tracks III: Proceedings of the 28th Symposium of the International Association of Vehicle System Dynamics, IAVSD 2023, August 21–25, 2023, Ottawa, Canada - Volume 2: Road Vehicles 176-184* (2024). (Lecture Notes in Mechanical Engineering (LNME)). Springer. Available from: https://doi.org/10.1007/978-3-031-66968-2_18.
- [41] Edwards CH. *Advanced Calculus of Several Variables, Vol. III – Successive Approximations and Implicit Functions*. Academic Press (1973).
- [42] Lunardi A. *Analytic Semigroups and Optimal Regularity in Parabolic Problems*. 1st ed. Birkhäuser Basel (1995).
- [43] Romano L, Aamo OM, Åslund J, Frisk E. Linear viscoelastic rheological FrBD models. Submitted to *IEEE Control Syst Lett* (2025).
- [44] Romano L, Timpone F, Bruzelius F, Jacobson B. Transient Tire Slip Losses Using the Brush Theory. *Tire Science And Technology* 52(1):51-75 (2024). Available from: <https://doi.org/10.2346/tire.22.20002>.
- [45] Kobayashi T, Katsuyama E, Sugiura H, et al. Direct yaw moment control and power consumption of in-wheel motor vehicle in steady state turning. *Veh Syst Dyn*. 2017;55(1):104–120. Available from: <https://doi.org/10.1080/00423114.2016.1246737>.
- [46] Kobayashi T, Katsuyama E, Sugiura H, et al. Efficient direct yaw moment control: tyre slip power loss minimization for four-independent wheel drive vehicle. *Veh Syst Dyn*. 2018;56(5):719–733. Available from: <https://doi.org/10.1080/00423114.2017.1330483>.
- [47] Kobayashi T, Katsuyama E, Sugiura H, Hattori H, Ono E, Yamamoto M. Theoretical analysis of tyre slip power dissipation mechanism using brush model. *Vehicle Syst. Dyn*. 2020;58(8):1242-1256. Available from <https://doi.org/10.1080/00423114.2019.1612926>.
- [48] van Blijderveen D. Longitudinal slip actuation of the flat plank tire tester, DC 2022.005, Master’s thesis TU Eindhoven (2022).
- [49] Aertssen AJ. Flat plank tire tester enhancements for transient measurements and model parametrization, DC 2023.028, Master’s thesis, TU Eindhoven (2023).